iScience

CellPress

Article

A Cocrystal Precursor Strategy for Carbon-Rich Graphitic Carbon Nitride toward High-Efficiency Photocatalytic Overall Water Splitting

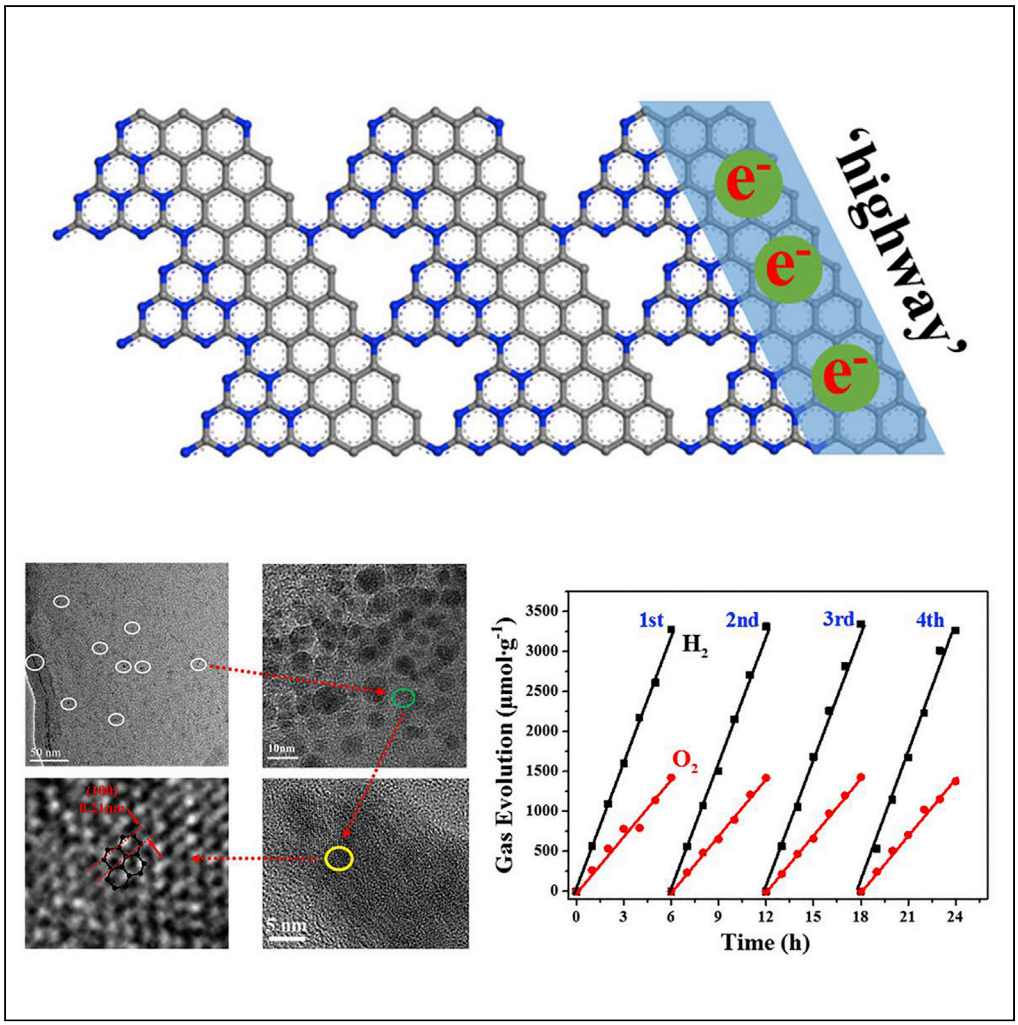

Xiaoyu Fang, Rui Gao, Yongsheng Yang, Dongpeng Yan

yandp@bnu.edu.cn

HIGHLIGHTS

Cocrystal precursor results in high dispersion of active sites at molecular level

Carbon units drive the separation and transmission of photogenerated electrons

C_{co}-C_3N_4 exhibits high catalytic activity without sacrificial reagent or co-catalyst

Fang et al., iScience 16, 22–30 June 28, 2019
https://doi.org/10.1016/j.isci.2019.05.015

iScience

CellPress

Article

A Cocrystal Precursor Strategy for Carbon-Rich Graphitic Carbon Nitride toward High-Efficiency Photocatalytic Overall Water Splitting

Xiaoyu Fang,[1] Rui Gao,[2] Yongsheng Yang,[1,3] and Dongpeng Yan[1,2,4,*]

SUMMARY

Direct and efficient photocatalytic overall water splitting is crucial for the sustainable conversion and storage of renewable solar energy. Herein, we present the design of a carbon-rich graphitic carbon nitride (C_{co}-C_3N_4), prepared from a layered molecular cocrystal precursor. The cocrystal microsheets were synthesized using a facile hydrothermal process. Following two-step thermal treatment and liquid exfoliation, the product maintains the 2D morphology owing to the toptactic transformation process. The C_{co}-C_3N_4 exhibits an enhanced photogenerated electron-hole separation, high charge transport capacity, and prolonged lifetime of the carriers, relative to the g-C_3N_4 system. In the absence of any sacrificial reagent or co-catalyst, the C_{co}-C_3N_4 microsheets exhibit a high photocatalytic activity. The work presented in this report supplies a cocrystal route for the orderly molecular self-assembly of precursor materials to tailor the chemical compositions and electronic structures. Moreover, the generation of a highly efficient water-splitting photocatalyst has larger implications for sustainable energy applications.

INTRODUCTION

Recent efforts toward the direct conversion of solar energy into chemical fuels have been faced with challenges with regard to effective energy conversion and environmental protection (Kudo and Miseki, 2009; Walter et al., 2010; Chen et al., 2010). Of the currently employed green strategies for energy conversion, the use of sunlight to directly split water into H_2 and O_2 is believed to have the most potential (Tada et al., 2006; Kageshima et al., 2016; Liang et al., 2016). The sunlight-driven water-splitting process sequentially undergoes three steps: (1) light harvesting, (2) separation and transport of the photogenerated carrier, and (3) surface redox (Kudo and Miseki, 2009; Xiang et al., 2012). Consequently, efficient photocatalysts usually feature favorable band gap energies and minimal recombination of the photocarriers (Shown et al., 2018; Asahi et al., 2001; Yamada et al., 2014). However, many of the current photocatalytic systems require the use of sacrificial reagents and co-catalysts to bolster catalytic performance, presenting a liability in the case wherein the photogenerated electrons or holes react preferentially with the sacrificial reagents or co-catalysts (Yao et al., 2016). Therefore it is highly desirable to develop suitable photocatalysts, which are capable of facilitating the overall water splitting in the absence of sacrificial reagents and co-catalysts (Zhang et al., 2016).

Although several well-developed inorganic semiconductors (such as TiO_2, Ni et al., 2007; $BiVO_4$, Kim and Choi, 2014; and Fe_2O_3, Sivula et al., 2011) have drawn great interest in the field of photocatalysis, the efficiency and stability of these materials is still far from the requirement of overall water splitting. Efforts to develop robust visible-light-active photocatalysts identified a polymeric semiconductor derived from small molecules (such as melamine and urea), namely, graphitic carbon nitride (g-C_3N_4), which has elicited ripples of excitement in the research communities as a promising next-generation metal-free photocatalyst, owing to its facile synthesis, favorable electronic structure, high physicochemical stability, and earth-abundant nature (Cao et al., 2015; Zhang et al., 2011; Wang et al., 2009; Liu et al., 2015). The unique properties of metal-free g-C_3N_4 allow for its use in a diverse range of applications, including photocatalytic hydrogen evolution (Duan et al., 2015), the oxygen reduction reaction (Yu et al., 2016), and the oxygen evolution reaction (Arif et al., 2018). However, the photocatalytic performance of g-C_3N_4 has been restricted by its low-wavelength absorption, fast recombination of carriers, and weak electronic conductivity (Dai et al., 2014; Niu et al., 2012; Che et al., 2017). Strategies that have been employed to address these challenges include the introduction of mesopores (Hao et al., 2016), engineering of micro- or nanostructure (Guo

[1]Beijing Key Laboratory of Energy Conversion and Storage Materials College of Chemistry, Beijing Normal University, Beijing 100875, P. R. China

[2]State Key Laboratory of Chemical Resource Engineering, Beijing University of Chemical Technology, Beijing 100029, P. R. China

[3]Institute of Catalysis for Energy and Environment, College of Chemistry and Chemical Engineering, Shenyang Normal University, Shenyang 110034, P. R. China

[4]Lead Contact

*Correspondence: yandp@bnu.edu.cn

https://doi.org/10.1016/j.isci.2019.05.015

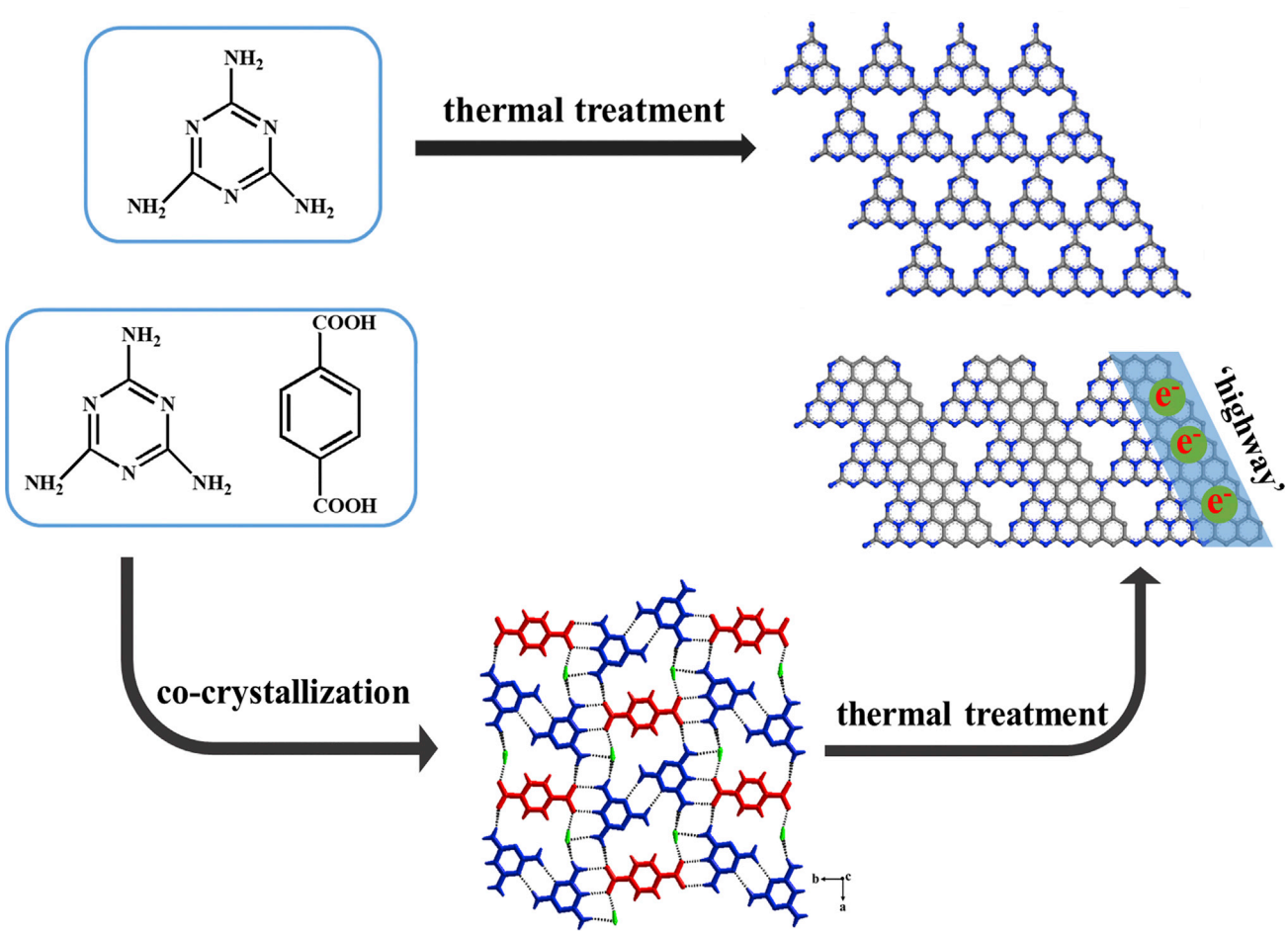

Figure 1. The Formation Process of the Pristine g-C_3N_4 and C_{co}-C_3N_4

et al., 2016), hybridization with semiconductor (Liao et al., 2012), deposition by noble metal (Zhu et al., 2016), and doping with metals or non-metals (Liu et al., 2010). Moreover, stitching together two-dimensional (2D) domains featuring similar aromatic structures (e.g., a graphitic carbon ring unit) via continuous π-conjugation provides a method for tuning the band structure and electronic transport properties and results in unimpeded in-plane electron-hole separation and charge transfer processes (Che et al., 2017; Liao et al., 2012; Du et al., 2012; Gong et al., 2014; Huang et al., 2015). Despite great advancements in the g-C_3N_4-based photocatalysts, the tailoring of the π-conjugated sections in-plane in carbon nitride for achieving minimized recombination and the ordered movement of photocarriers to suitable redox sites remains elusive.

The term cocrystal usually refers to a molecular solid composed of at least two types of molecular units, organized by non-covalent interactions (Etter et al., 1989). We hypothesized that polymerization of a cocrystal precursor could be employed to generate carbon nitride materials featuring desirable molecular sections and suitable C/N ratios, aided by the modular design and facile preparation of the cocrystallization process (Fang et al., 2017; Yan and Evans, 2014). Moreover, the toptactic conversion of the orderly molecular assembly from the cocrystal to carbon nitride may result in the high dispersion of catalytic sites at the molecular level requisite for high-efficiency water-splitting applications. In this work, we selected terephthalic acid (TPA) and melamine (MA) to build cocrystals, as the hydrogen-bonding interaction between –COOH functionality in TPA and the –NH_2 group in MA facilitates the formation of 2D molecular sheets (Figure 1). Furthermore, the capacity of aromatic TPA for π-conjugation is amenable to the introduction of ordered carbon-rich frameworks for effective photogenerated carrier separation and transport. The resulting carbon-rich graphitic carbon nitride yields a high photocatalytic activity with simultaneous

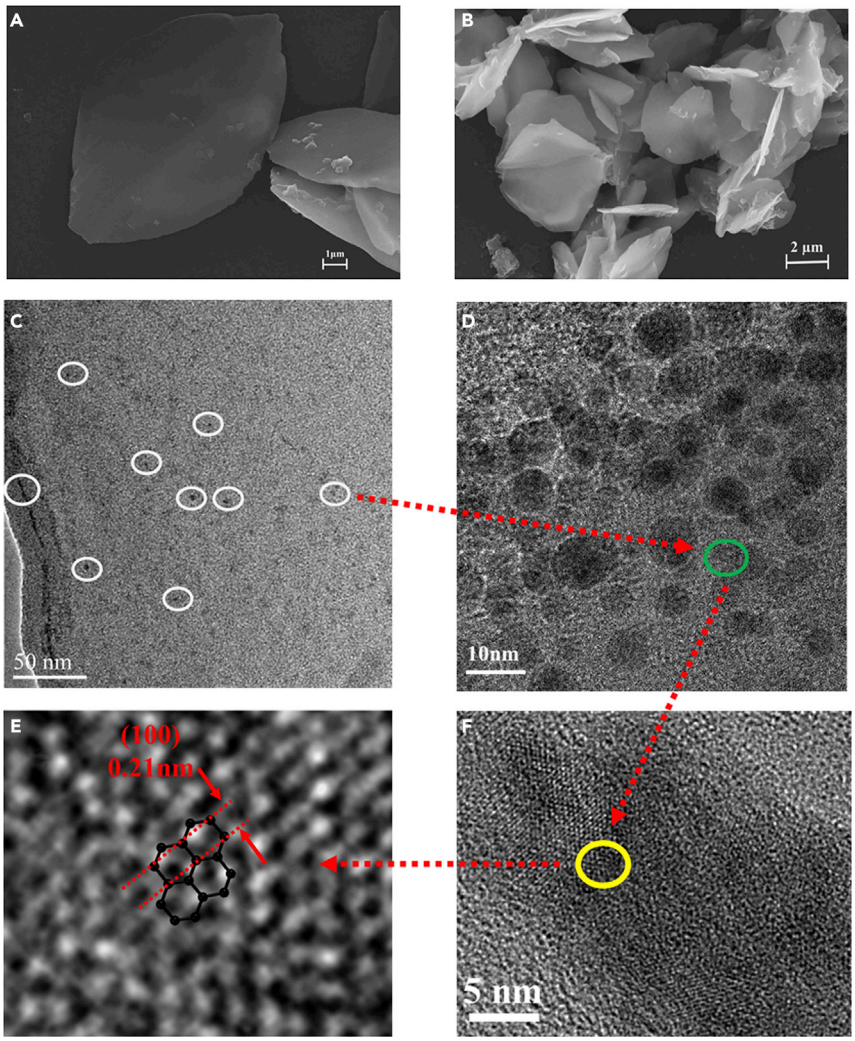

Figure 2. Morphology Images for Cocrystal Precursor and C_{co}-C_3N_4

(A and B) SEM images for cocrystal precursor (A) and C_{co}-C_3N_4 (B).

(C–F) High-resolution TEM image for C_{co}-C_3N_4 nanosheets in different scales at the same area.

production of H_2 and O_2 at rates up to 530 and 255 $\mu mol \cdot g^{-1} \cdot h^{-1}$, respectively, which exceeds those of most reported current metal-free photocatalysts. The work presented herein not only establishes a cocrystal precursor method for extending the diversity of the chemical structure and composition of graphitic carbon nitride materials but also demonstrates their applicability as efficient water-splitting photocatalysts.

RESULTS AND DISCUSSION

The cocrystal composed of a 2:1 ratio of MA and TPA was prepared using a hydrothermal method at 140°C. Details of the crystal are summarized in Table S1. The X-ray diffraction (XRD) pattern of the resultant 2MA.TPA sample is consistent with the simulated result, confirming high purity of the cocrystal product (Figure S1A). The crystal structure illustrates that, in a single layer, the electrostatic and hydrogen bonding interactions drive the cooperative assembly of protonated melamine, terephthalic acid, and H_2O into the 2D supramolecular pattern. Besides, the molecular sheets orient perpendicularly through π-π interaction and hydrogen bonds (Figures S1B and S1C), with an interlayer spacing of approximately 1 nm. Scanning electron microscopic (SEM) imaging of the surface (Figures 2A and S1D) reveals the presence of typical 2D microsheet morphologies in the 2MA.TPA cocrystal, consistent with the layered structure observed by XRD. Following a two-step thermal treatment, the cocrystal product presents the same XRD pattern and Fourier transform infrared bands with the typical g-C_3N_4 structural features (Figures S5 and S6A),

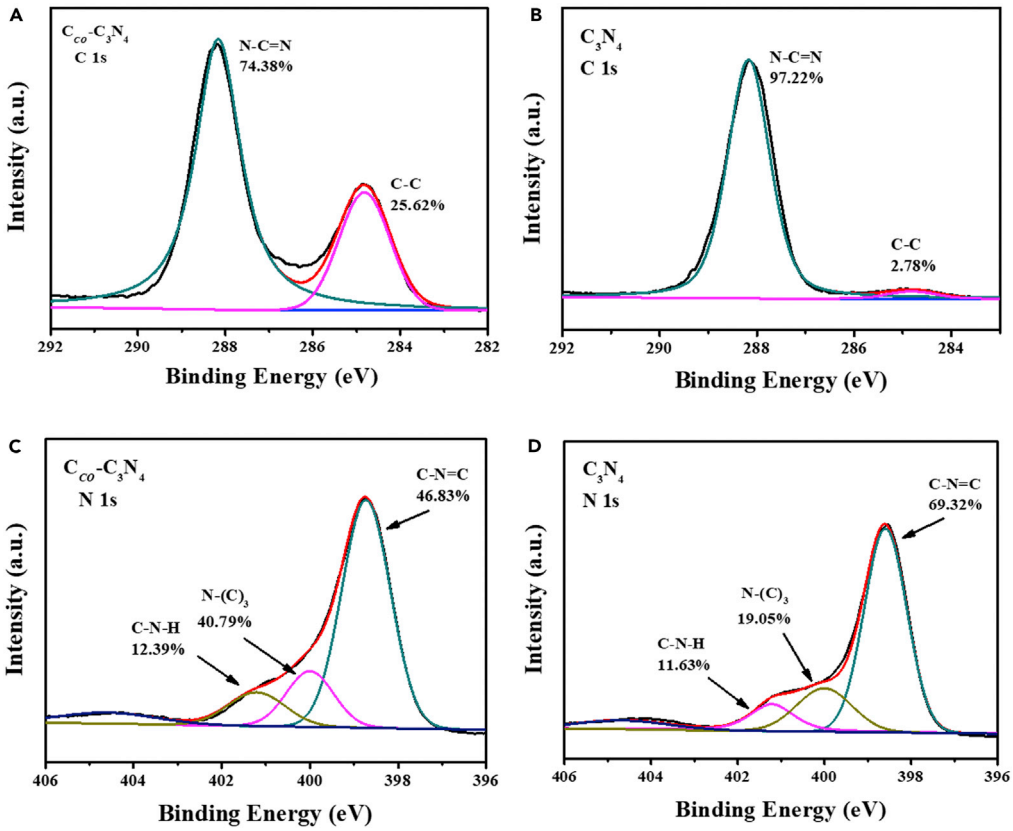

Figure 3. X-ray Photoelectron Spectroscopy for C_{co}-C_3N_4 and g-C_3N_4

(A and B) C 1s high-resolution X-ray photoelectron spectroscopy (XPS) spectra for C_{co}-C_3N_4 (A) and pristine g-C_3N_4 (B). (C and D) N 1s high-resolution XPS spectra for C_{co}-C_3N_4 (C) and pristine g-C_3N_4 (D).

indicating the successful formation of graphitic carbon nitride (denoted as C_{co}-C_3N_4 hereafter). The color of C_{co}-C_3N_4 is brown, which is different from that of the pristine g-C_3N_4 (Figure S2). Elemental analysis and energy-dispersive X-ray spectra (Figure S7) measured a C/N ratio of approximately 7:3 for the C_{co}-C_3N_4 product, suggesting its carbon-rich characteristics through the cocrystal precursor method. The C/N ratio is also in agreement with the idealized model derived for the C_{co}-C_3N_4. The SEM images (Figures 2A, 2B, and S3) indicate that the C_{co}-C_3N_4 maintains sheet-like characteristics, suggestive of a topotactic transformation from the initial 2D microsheets of the cocrystal.

After grinding the synthesized cocrystal into fine powders and dispersing the resultant particles using ultrasonic waves, homogeneous C_{co}-C_3N_4 microsheets can be observed, as illustrated in the transmission electron microscopic (TEM) image (Figure S4A), which is almost the same as the pristine g-C_3N_4 (Figure S4B). A high-magnification image reveals that there is no obvious nanoparticle formation on the smooth surface. The high-resolution TEM images (Figures 2C–2F) exhibit considerable apparent lattice fringe regions randomly incorporated throughout the disordered basal plane domain of the g-C_3N_4 matrix. The corresponding lattice fringes of 0.21 nm are ascribed to the (100) planes of graphite. The observed hexagonal pattern is attributed to the incorporated carbon ring and/or triazine frameworks (Che et al., 2017). The presence of crystal defect sites, created during thermal treatment, is manifest in breaks in the hexagonal pattern.

X-ray photoelectron spectroscopy was used to analyze the composition and chemical environment of both the prepared C_{co}-C_3N_4 and pristine g-C_3N_4 (Figure 3). In the C 1s spectrum of C_{co}-C_3N_4, two major peaks at 288.17 and 284.82 eV were assigned to the sp^2-hybridized carbons in the heterocyclic aromatic ring (N–C=N) and the graphitic carbon (C–C), respectively (Hammer et al., 1998). Compared with the pristine g-C_3N_4, the graphitic carbon (C–C) units in the spectrum of C_{co}-C_3N_4 have been highly enhanced, and

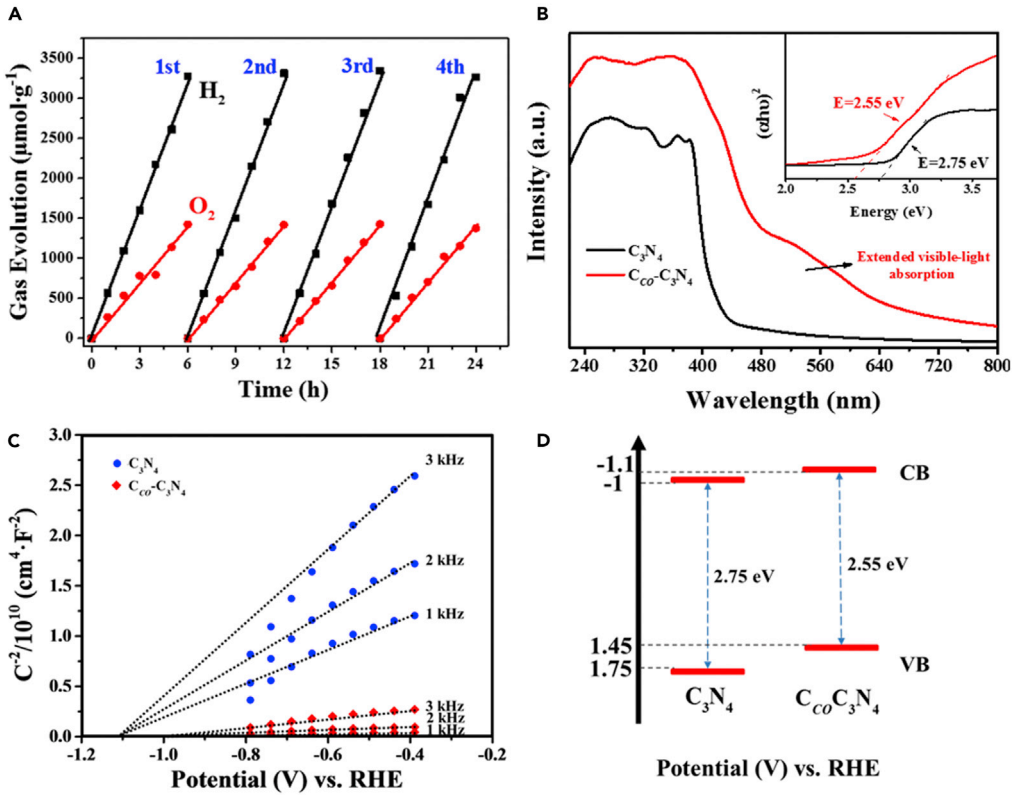

Figure 4. The Characterization of Overall Water Splitting for C_{co}-C_3N_4

(A) Typical time course of H_2 and O_2 evolution for C_{co}-C_3N_4.

(B) UV-vis absorption and corresponding Tauc/Davis-Mott plots.

(C) Mott-Schottky plots.

(D) Band structure diagram of C_{co}-C_3N_4 and g-C_3N_4 polymers calculated by optical absorption and typical electrochemical Mott-Schottky methods.

the ratio of triazine units to carbon-ring can be estimated at around 3:1. In the N 1s spectrum of C_{co}-C_3N_4, evidently, the intense and broad peak ranging from 396 to 402.7 eV can be deconvoluted into three peaks, including 398.59 eV for sp^2-hybridized nitrogen in triazine rings (C–N=C), 400.0 eV for tertiary nitrogen N–$(C)_3$ groups, and 401.21 eV for amino functions carrying hydrogen (C–N–H) (Hammer et al., 1998). A small peak observed at 404.66 eV in the N 1s spectrum is attributed to a positive charge localization in the heterojunction (Che et al., 2017). Usually, several peaks can be detected in bulk g-C_3N_4 (Li et al., 2012). As shown in the Raman spectra (Figure S6B), an obviously wide peak from g-C_3N_4 is observed at *ca.* 1,550 cm^{-1}, which indicates that the bulk g-C_3N_4 has been well exfoliated into thin nanosheets (Jiang et al., 2014). Meanwhile, a similarly wide band can be observed in the C_{co}-C_3N_4, which is also due to the exfoliated nanosheets as observed by TEM above. Moreover, two peaks at 1,343 and 1,590 cm^{-1} were detected, corresponding to the D and G bands of graphene-based nanomaterials, respectively (Ma et al., 2017). Collectively, these spectra demonstrate the successful formation of the g-C_3N_4-based heterostructures via the incorporation of carbon ring.

To test the photocatalytic activity, we evaluated the water-splitting performance of the C_{co}-C_3N_4 microsheets dispersed in pure water in the absence of sacrificial reagents or co-catalysts under standard reaction and measurement conditions. Simultaneous evolution of H_2 and O_2 gases was detected in a ratio of approximately 2:1 for the C_{co}-C_3N_4, and the corresponding H_2 and O_2 evolution rates are up to 530 and 255 $\mu mol \cdot g^{-1} \cdot h^{-1}$, respectively (Figure 4A). As is shown in Figure S9, the quantum efficiency of C_{co}-C_3N_4 reaches up to 5.28% at 400 nm. As a control experiment, the photocatalytic activity of pristine g-C_3N_4 was tested under the same experimental condition. In this case, no H_2 or O_2 evolution was detected, which may be attributed to the gas production below the detection limit.

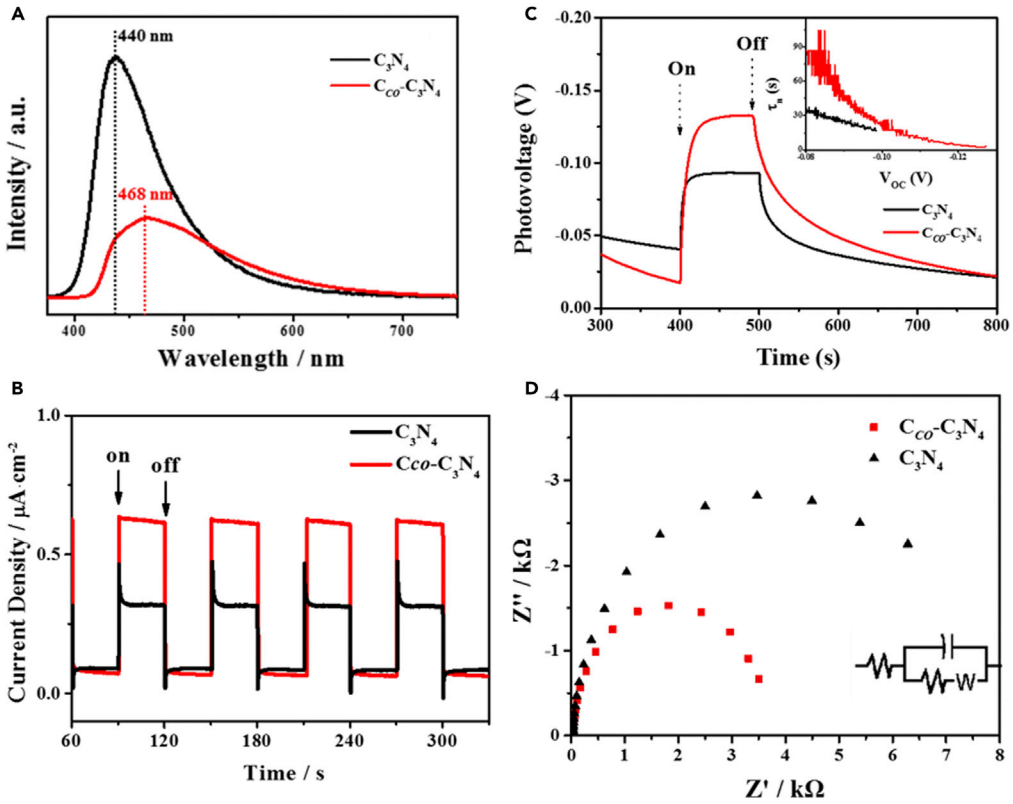

Figure 5. The Performance Comparison between C_{co}-C_3N_4 and g-C_3N_4

(A) Photoluminescence emission curves.

(B) Transient photocurrent responses of C_{co}-C_3N_4 and g-C_3N_4 under visible light irradiation.

(C) Transient open-circuit voltage decay (OCVD) measurement, and inset depicting the average lifetimes of the photogenerated carriers (τ_n) obtained from the OCVD measurement.

(D) Electrochemical impedance spectra (EIS) and insets showing the equivalent circuit impedance mode.

To gain insight into the superior photocatalytic activity of C_{co}-C_3N_4, the electronic structure of this material was studied. Ultraviolet-visible (UV-vis) light absorption spectra were analyzed to determine the band gap (Figure 4B). The pristine g-C_3N_4 exhibits an intrinsic absorption edge near 460 nm, corresponding to a calculated band gap of about 2.75 eV according to the Kubelka-Munk function. A similar absorption edge was observed for the C_{co}-C_3N_4 microsheets; however, an extended visible light absorption over 500–800 nm is also detected, which suggests the accessibility of low-energy visible light. The UV-vis spectrum appearing between 480 and 600 nm signifies the existence of an Urbach band tail. This suggests that the integration of carbon-rich units into g-C_3N_4 has imported a new intermediate energy level, which is consistent with the decreased band gap. Moreover, a good linear fit is obtained using $(\alpha h\nu)^2$ for Tauc plots, indicating direct band gap semiconductor behavior for C_{co}-C_3N_4. The band gap of C_{co}-C_3N_4 is evaluated as 2.55 eV, corresponding to the extended visible light absorption. The decrease in band gap energy relative to the pristine g-C_3N_4 is consistent with the introduction of the carbon-rich units in the C_{co}-C_3N_4 matrix. This is because the graphitic structure possesses strong absorption in the visible light region, contributing to the great light-harvesting efficiency of the heterostructure. Consequently, the range of UV-vis absorption has been broadened (Che et al., 2017; Liao et al., 2012; Du et al., 2012). Based on electrochemical Mott-Schottky plots (Figure 4C), the conduction band minimum and valence band maximum of the C_{co}-C_3N_4 can be determined as −1.1 and 1.45 eV versus reversible hydrogen electrode, respectively. The redox potential of C_{co}-C_3N_4 is reductively shifted relative to pristine g-C_3N_4 (−1 eV), which supports the redox shuttling behavior of C_{co}-C_3N_4 in the water-splitting reaction (Figure 4D).

Photoluminescence (PL) emission is useful to probe the efficiency of electron-hole pair trapping, migration, and transfer in the semiconductor material. Relative to the pristine g-C_3N_4, which produces an emission at *ca.* 440 nm (Figure 5A), the C_{co}-C_3N_4 exhibits an obvious red-shifted emission occurring at 468 nm.

The observed energy shift of emission is attributed to the enhanced graphitic carbon sections and extended visible absorption as described above. The PL intensity of C_{co}-C_3N_4 is diminished relative to pristine g-C_3N_4, which confirms a decreased electron-hole recombination rate for C_{co}-C_3N_4. To gain more insight into the information on charge separation ability in the C_{co}-C_3N_4 matrix, the PL decay spectra were performed on both the pristine g-C_3N_4 and C_{co}-C_3N_4 (Figure S8). The PL lifetimes of pristine g-C_3N_4 and C_{co}-C_3N_4 are retrieved to be 3.41 and 18.14 ns, respectively. Obviously, C_{co}-C_3N_4 has a longer PL lifetime, suggesting that the formed carbon-rich units and heterostructure interface speed up the photogenerated charge transfer and effectively depresses charge recombination (Yue et al., 2017a, 2017b). Moreover, a comparison of the photocurrent-time curves obtained by subjecting g-C_3N_4 and C_{co}-C_3N_4 to typical on-off cycles of visible light irradiation shows an enhanced photocurrent response for C_{co}-C_3N_4 (Figure 5B), nearly two times that of the pristine g-C_3N_4. Notably, the pristine g-C_3N_4 exhibits an anodic photocurrent spike upon initial irradiation, followed by decay of the photocurrent until a constant current is reached. The observed decrease in photocurrent is attributed to the accumulation of photogenerated holes on the g-C_3N_4 surface and the competitive recombination of these holes with electrons or reduced species in the electrolyte. Following equilibration of the competitive separation and recombination of electron-hole pairs, a constant photocurrent is achieved. Similar behavior has been observed in a previously reported g-C_3N_4 system (Ran et al., 2018). In contrast, little to no anodic photocurrent spike is observed for C_{co}-C_3N_4. The alternation of the photoelectron transfer behavior suggests that the C_{co}-C_3N_4 could obviously enhance the separation of photogenerated carriers. We hypothesize that the introduced carbon rings of C_{co}-C_3N_4 act as a highway for electron transfer, allowing the photogenerated electrons to rapidly traverse the material while the photogenerated holes rest on melem units. In short, the mobility of the photoexcited charge carriers is highly promoted.

The transient open-circuit voltage decay measurements (Figure 5C) indicate that the C_{co}-C_3N_4 holds a higher open-circuit voltage and slower photovoltage decay behavior upon light cycling. These properties suggest a higher energy and longer lifetime of the photoexcited carriers. Moreover, the average lifetime of the photocarriers in C_{co}-C_3N_4 is prolonged by nearly three orders of magnitude relative to that of pristine g-C_3N_4 (the inset of Figure 5C). The prolonged lifetime of the photogenerated carriers, in combination with the enhanced electron mobility and higher work function, enables the C_{co}-C_3N_4 to trap photoexcited electrons and suppress electron-hole recombination more effectively than the pristine g-C_3N_4. Furthermore, the Nyquist plots for C_{co}-C_3N_4 catalysts illustrate low charge transfer resistance relative to that of g-C_3N_4 (Figure 5D). The aforementioned results indicate that the electronic structure of C_{co}-C_3N_4 has been greatly modified by grafted carbon rings, leading to efficient photoexcited electron-hole separation and longer lifetime of the photocarriers.

Conclusion

In summary, we have prepared a C_{co}-C_3N_4 heterostructure with uniform introduction of graphitic carbon rings into the typical g-C_3N_4 using a facile cocrystallization method. The resultant material achieves highly efficient photoexcited electron-hole separation and superior charge transport behavior relative to the pristine g-C_3N_4. In addition, the C_{co}-C_3N_4 can effectively facilitate the overall water-splitting reaction under light irradiation with the prominent H_2 and O_2 production rates up to 530 and 255 $\mu mol \cdot g^{-1} \cdot h^{-1}$, respectively. It is noted that the photocatalytic water-splitting activity surpasses majority of the currently reported photocatalysts, with hydrogen evolution under the full solar spectrum (Table S2). Moreover, the water-splitting activity is achieved in the absence of sacrificial reagents and co-catalysts, supporting metal-free photocatalysis. The highly efficient and simultaneous production of O_2 and H_2 is attributed to the enhanced generation and mobility of the photoexcited charge carriers upon introduction of the carbon-rich graphitic carbon units. The extension of the cocrystal precursor method presented in this report for the fabrication of other energy-matched semiconductor systems will have larger implications in the development of materials for applications in solar energy conversion.

Limitations of the Study

More systematic and detailed theoretical calculations on the relationships between the structure and its overall water-splitting performance are required for further study. To achieve practical application of the metal-free materials, considerable work needs to be done.

METHODS

All methods can be found in the accompanying Transparent Methods supplemental file.

SUPPLEMENTAL INFORMATION

Supplemental Information can be found online at https://doi.org/10.1016/j.isci.2019.05.015.

ACKNOWLEDGMENTS

This work was supported by the National Natural Science Foundation of China (Grants No. 21771021 and 21822501), the 973 Program (Grant No. 2014CB932103), the Beijing Nova Program (xx2018115), the Fundamental Research Funds for the Central Universities, and Analytical and Measurements Fund of Beijing Normal University.

AUTHOR CONTRIBUTIONS

D.Y. and X.F. designed the project. X.F. synthesized the catalysts and carried out the photocatalytic measurements. X.F., R.G., Y.Y., and D.Y. carried out the data analysis. X.F. and D.Y. co-wrote the manuscript.

DECLARATION OF INTERESTS

The authors declare no competing interests.

Received: October 24, 2018
Revised: February 6, 2019
Accepted: May 9, 2019
Published: June 28, 2019

REFERENCES

Arif, M., Yasin, G., Shakeel, M., Fang, X., Gao, R., Ji, S., and Yan, D. (2018). Coupling of bifunctional CoMn-layered double hydroxide@graphitic C_3N_4 nanohybrids towards efficient photoelectrochemical overall water splitting. Chem. Asian J. *13*, 1045–1052.

Asahi, R., Morikawa, T., Ohwaki, T., Aoki, K., and Taga, Y. (2001). Visible-light photocatalysis in nitrogen-doped titanium oxides. Science *293*, 269–271.

Cao, S., Low, J., Yu, J., and Jaroniec, M. (2015). Polymeric photocatalysts based on graphitic carbon nitride. Adv. Mater. *27*, 2150–2176.

Che, W., Cheng, W., Yao, T., Tang, F., Liu, W., Su, H., Huang, Y., Liu, Q., Liu, J., Hu, F., et al. (2017). Fast photoelectron transfer in (C_{ring})-C_3N_4 plane heterostructural nanosheets for overall water splitting. J. Am. Chem. Soc. *139*, 3021–3026.

Chen, X., Shen, S., Guo, L., and Mao, S.S. (2010). Semiconductor-based photocatalytic hydrogen generation. Chem. Rev. *110*, 6503–6570.

Dai, K., Lu, L., Liang, C., Liu, Q., and Zhu, G. (2014). Heterojunction of facet coupled g-C_3N_4/surface-fluorinated TiO_2 nanosheets for organic pollutants degradation under visible LED light irradiation. Appl. Catal. B *156*, 331–340.

Du, A.J., Sanvito, S., Li, Z., Wang, D.W., Jiao, Y., Liao, T., Sun, Q., Ng, Y.H., Zhu, Z.H., Amal, R., and Smith, S.C. (2012). Hybrid graphene and graphitic carbon nitride nanocomposite: gap opening, electron-hole puddle, interfacial charge transfer, and enhanced visible light response. J. Am. Chem. Soc. *134*, 4393–4397.

Duan, J., Chen, S., Jaroniec, M., and Qiao, S.Z. (2015). Porous C_3N_4 nanolayers@N-graphene films as catalyst electrodes for highly efficient hydrogen evolution. ACS Nano *9*, 931–940.

Etter, M.C., Frankenbach, G.M., and Bernstein, J. (1989). Solid-state nucleophilic aromatic substitution reaction of a carboxylic acid cocrystal. Tetrahedron Lett. *30*, 3617–3620.

Fang, X., Yang, X., and Yan, D. (2017). Vapor-phase π–π molecular recognition: a fast and solvent-free strategy towards the formation of co-crystalline hollow microtube with 1D optical waveguide and up-conversion emission. J. Mater. Chem. C *5*, 1632–1637.

Gong, Y.J., Lin, J.H., Wang, X.L., Shi, G., Lei, S.D., Lin, Z., Zou, X.L., Ye, G.L., Vajtai, R., Yakobson, B.I., et al. (2014). Vertical and in-plane heterostructures from WS_2/MoS_2 monolayers. Nat. Mater. *13*, 1135–1142.

Guo, S., Deng, Z., Li, M., Jiang, B., Tian, C., Pan, Q., and Fu, H. (2016). Phosphorus-doped carbon nitride tubes with a layered micro-nanostructure for enhanced visible-light photocatalytic hydrogen evolution. Angew. Chem. Int. Ed. *55*, 1830–1834.

Hammer, P., Victoria, N.M., and Alvarez, F. (1998). Electronic structure of hydrogenated carbon nitride films. J. Vac. Sci. Technol. A *16*, 2941–2949.

Hao, R., Wang, G., Tang, H., Sun, L., Xu, C., and Han, D. (2016). Template-free preparation of macro/mesoporous g-C_3N_4/TiO_2 heterojunction photocatalysts with enhanced visible light photocatalytic activity. Appl. Catal. B *187*, 47–58.

Huang, C.J., Chen, C., Zhang, M.W., Lin, L.H., Ye, X.X., Lin, S., Antonietti, M., and Wang, X.C. (2015). Carbon-doped BN nanosheets for metal-free photoredox catalysis. Nat. Commun. *6*, 7698.

Jiang, J., Lei, O.Y., Zhu, L., Zheng, A., Zou, J., Yi, X., and Tang, H. (2014). Dependence of electronic structure of g-C_3N_4 on the layer number of its nanosheets: a study by Raman spectroscopy coupled with first-principles calculations. Carbon *80*, 213–221.

Kageshima, Y., Shinagawa, T., Kuwata, T., Nakata, J., Minegishi, T., Takanabe, K., and Domen, K. (2016). A miniature solar device for overall water splitting consisting of series-connected spherical silicon solar cells. Sci. Rep. *6*, 24633.

Kim, T.W., and Choi, K.S. (2014). Nanoporous $BiVO_4$ photoanodes with dual-layer oxygen evolution catalysts for solar water splitting. Science *343*, 990–994.

Kudo, A., and Miseki, Y. (2009). Heterogeneous photocatalyst materials for water splitting. Chem. Soc. Rev. *38*, 253–278.

Li, J., Shen, B., Hong, Z., Lin, B., Gao, B., and Chen, Y. (2012). A facile approach to synthesize novel oxygen-doped g-C_3N_4 with superior visible-light photoreactivity. Chem. Commun. *48*, 12017–12019.

Liang, Y., Sun, X., Asiri, A.M., and He, Y. (2016). Amorphous Ni-B alloy nanoparticle film on Ni foam: rapid alternately dipping deposition for efficient overall water splitting. Nanotechnology *27*, 12LT01.

Liao, G., Chen, S., Quan, X., Yu, H., and Zhao, H. (2012). Graphene oxide modified g-C_3N_4

hybrid with enhanced photocatalytic capability under visible light irradiation. J. Mater. Chem. *22*, 2721–2726.

Liu, G., Niu, P., Sun, C., Smith, S.C., Chen, Z., Lu, G.Q., and Cheng, H.M. (2010). Unique electronic structure induced high photoreactivity of sulfur-doped graphitic C3N4. J. Am. Chem. Soc. *132*, 11642–11648.

Liu, J., Liu, Y., Liu, N., Han, Y., Zhang, X., Huang, H., Lifshitz, Y., Lee, S.T., Zhong, J., and Kang, Z. (2015). Metal-free efficient photocatalyst for stable visible water splitting via a two-electron pathway. Science *347*, 970–974.

Ma, D., Wu, J., Gao, M.C., Xin, Y.J., Sun, Y.Y., and Ma, T.J. (2017). Hydrothermal synthesis of an artificial Z-scheme visible light photocatalytic system using reduced graphene oxide as the electron mediator. Chem. Eng. J. *313*, 1567–1576.

Ni, M., Leung, M.K., Leung, D.Y., and Sumathy, K. (2007). A review and recent developments in photocatalytic water-splitting using TiO_2 for hydrogen production. Renew. Sustain. Energy Rev. *11*, 401–425.

Niu, P., Zhang, L., Liu, G., and Cheng, H.M. (2012). Graphene-like carbon nitride nanosheets for improved photocatalytic activities. Adv. Funct. Mater. *22*, 4763–4770.

Ran, J., Guo, W., Wang, H., Zhu, B., Yu, J., and Qiao, S.Z. (2018). Metal-Free 2D/2D phosphorene/g-C_3N_4 Van der Waals heterojunction for highly enhanced visible-light photocatalytic H_2 production. Adv. Mater. *30*, 1800128.

Shown, I., Samireddi, S., Chang, Y.C., Putikam, R., Chang, P.H., Sabbah, A., Fu, F.Y., Chen, W.F., Wu, C.I., Yu, T.Y., et al. (2018). Carbon-doped SnS_2 nanostructure as a high-efficiency solar fuel catalyst under visible light. Nat. Commun. *9*, 169.

Sivula, K., Le Formal, F., and Grätzel, M. (2011). Solar water splitting: progress using hematite (α-Fe_2O_3) photoelectrodes. ChemSusChem *4*, 432–449.

Tada, H., Mitsui, T., Kiyonaga, T., Akita, T., and Tanaka, K. (2006). All-solid-state Z-scheme in CdS-Au-TiO_2 three-component nanojunction system. Nat. Mater. *5*, 782.

Walter, M.G., Warren, E.L., McKone, J.R., Boettcher, S.W., Mi, Q., Santori, E.A., and Lewis, N.S. (2010). Solar water splitting cells. Chem. Rev. *110*, 6446–6473.

Wang, X., Maeda, K., Thomas, A., Takanabe, K., Xin, G., Carlsson, J.M., Domen, K., and Antonietti, M. (2009). A metal-free polymeric photocatalyst for hydrogen production from water under visible light. Nat. Mater. *8*, 76–80.

Xiang, Q., Yu, J., and Jaroniec, M. (2012). Graphene-based semiconductor photocatalysts. Chem. Soc. Rev. *41*, 782–796.

Yamada, Y., Nakamura, T., Endo, M., Wakamiya, A., and Kanemitsu, Y. (2014). Photocarrier recombination dynamics in perovskite $CH_3NH_3PbI_3$ for solar cell applications. J. Am. Chem. Soc. *136*, 11610–11613.

Yan, D., and Evans, D.G. (2014). Molecular crystalline materials with tunable luminescent properties: from polymorphs to multi-component solids. Mater. Horiz. *1*, 46–57.

Yao, L., Wei, D., Ni, Y., Yan, D., and Hu, C. (2016). Surface localization of CdZnS quantum dots onto 2D g-C_3N_4 ultrathin microribbons: highly efficient visible light-induced H_2-generation. Nano Energy *26*, 248–256.

Yu, H., Shang, L., Bian, T., Shi, R., Waterhouse, G.I., Zhao, Y., Zhou, C., Wu, L.Z., Tung, C.H., and Zhang, T. (2016). Nitrogen-doped porous carbon nanosheets templated from g-C_3N_4 as metal-free electrocatalysts for efficient oxygen reduction reaction. Adv. Mater. *28*, 5080–5086.

Yue, X., Yi, S., Wang, R., Zhang, Z., and Qiu, S. (2017a). Cobalt phosphide modified titanium oxide nanophotocatalysts with significantly enhanced photocatalytic hydrogen evolution from water splitting. Small *13*, 1603301.

Yue, X., Yi, S., Wang, R., Zhang, Z., and Qiu, S. (2017b). A novel architecture of dandelion-like Mo_2C/TiO_2 heterojunction photocatalysts towards high-performance photocatalytic hydrogen production from water splitting. J. Mater. Chem. A *5*, 10591–10598.

Zhang, Z., Long, J., Yang, L., Chen, W., Dai, W., Fu, X., and Wang, X. (2011). Organic semiconductor for artificial photosynthesis: water splitting into hydrogen by a bioinspired $C_3N_3S_3$ polymer under visible light irradiation. Chem. Sci. *2*, 1826–1830.

Zhang, G., Lan, Z.A., Lin, L., Lin, S., and Wang, X. (2016). Overall water splitting by Pt/g-C_3N_4 photocatalysts without using sacrificial agents. Chem. Sci. *7*, 3062–3066.

Zhu, Z., Lu, Z., Wang, D., Tang, X., Yan, Y., Shi, W., and Dong, H. (2016). Construction of high-dispersed Ag/Fe_3O_4/g-C_3N_4 photocatalyst by selective photo-deposition and improved photocatalytic activity. Appl. Catal. B *182*, 115–122.

ISCI, Volume *16*

Supplemental Information

A Cocrystal Precursor Strategy for Carbon-Rich Graphitic Carbon Nitride toward High-Efficiency Photocatalytic Overall Water Splitting

Xiaoyu Fang, Rui Gao, Yongsheng Yang, and Dongpeng Yan

Supporting Information

Title: A cocrystal precursor strategy for carbon-rich graphitic carbon nitride towards high-efficiency photocatalytic overall water splitting

Xiaoyu Fang, Rui Gao, Yongsheng Yang and Dongpeng Yan*

Table S1. Single crystal X-ray diffraction parameters of the cocrystal. Related to Figure 1.

Empirical formula	$C_7H_{11}N_6O_3$
Formula weight	227
Crystal system, space group	Monoclinic, *P*21/*c*
Unit cell dimensions	a = 6.7565 (10) **α = 90**
	b = 20.196 (4) **β = 92.153**
	c = 6.9648 (11) **γ = 90**
Volume	949.706

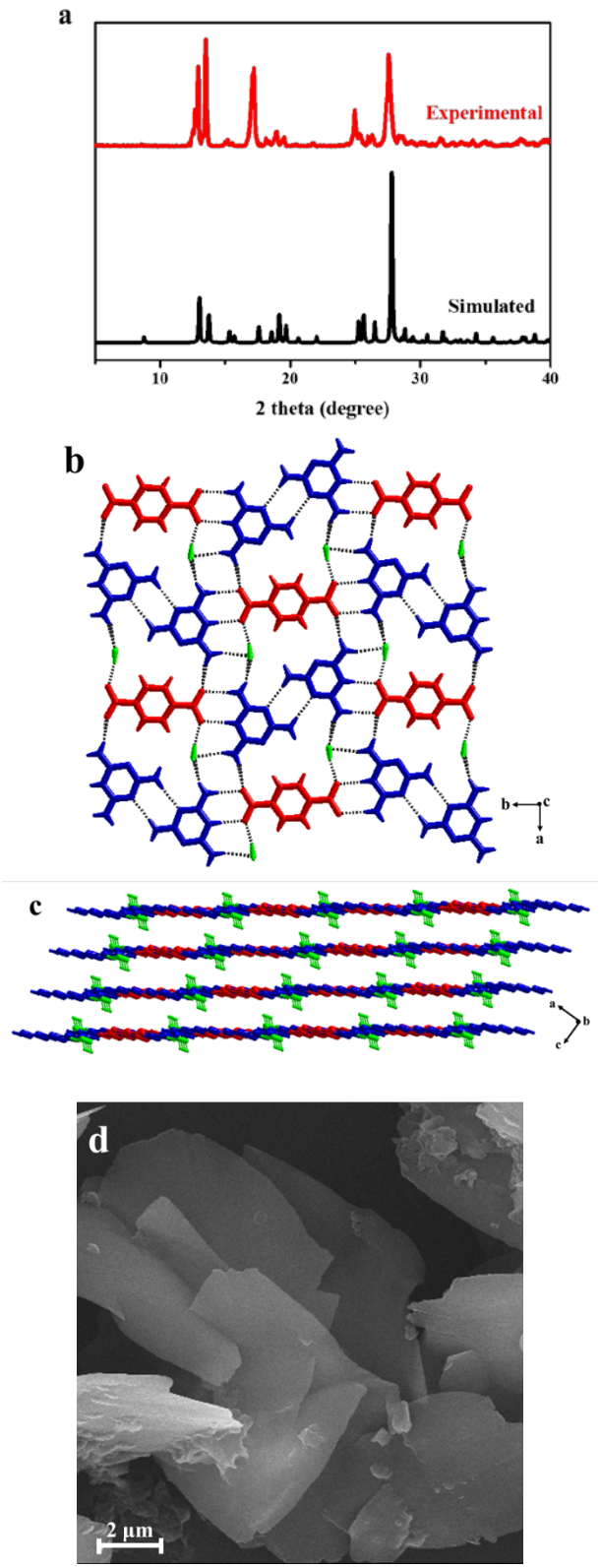

Figure S1. (a) Powder XRD pattern of the as-synthesized cocrystal. The experimental data is depicted in red, the simulated pattern in black. (b) A single layer of the cocrystal from the solid state structure. (c) π-π stacking in the cocrystal. In b and c, melamine is depicted in blue, terephthalic acid in red, and H_2O in green. Hydrogen bonding interactions are indicated with grey dashes. (d) The SEM image for cocrystal precursor. Related to Figure 1 and Figure 2.

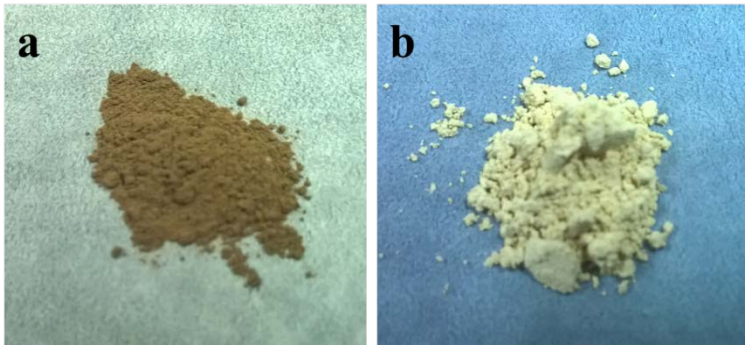

Figure S2. Optical photographs of C_{co}-C_3N_4, (a) and pristine g-C_3N_4 (b). Related to Figure 1 and Figure 3.

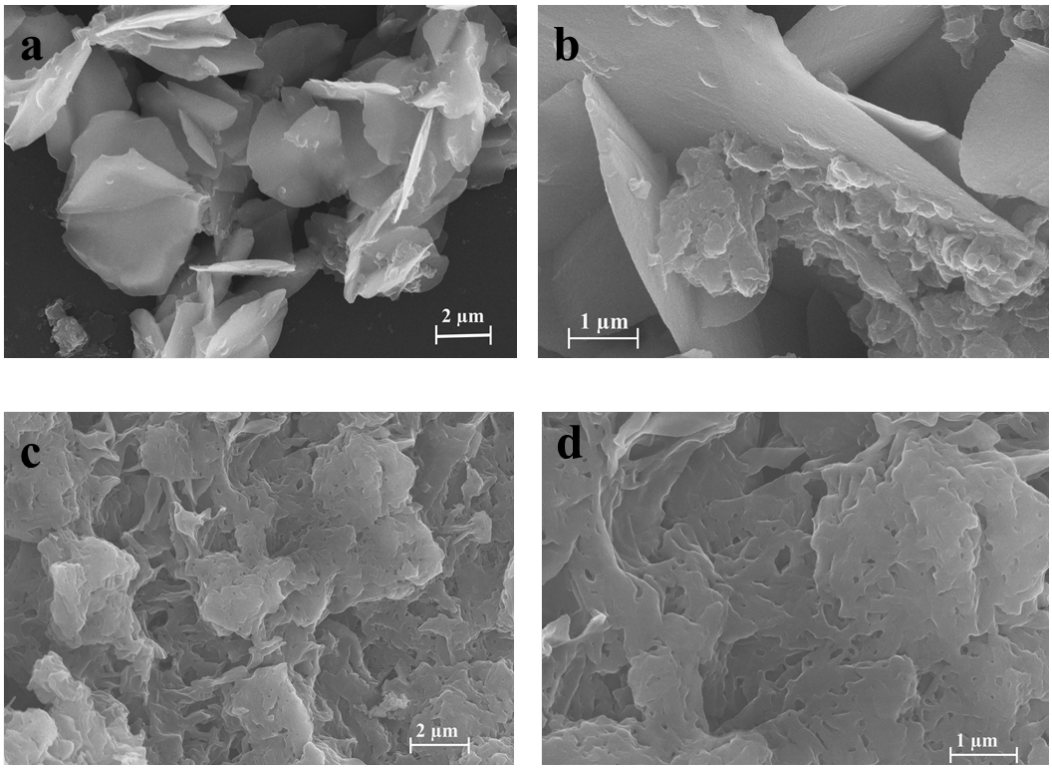

Figure S3. SEM images of the samples C_{co}-C_3N_4 (a) and (b) and pristine g-C_3N_4 (c) and (d). Related to Figure 2.

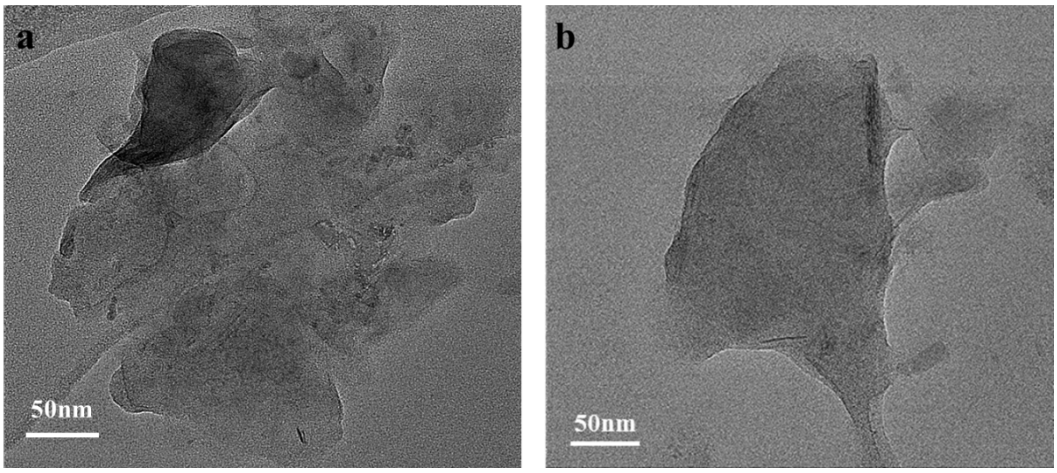

Figure S4. Representative TEM images of C_{co}-C_3N_4 (a) and pristine C_3N_4 (b). Related to Figure 2.

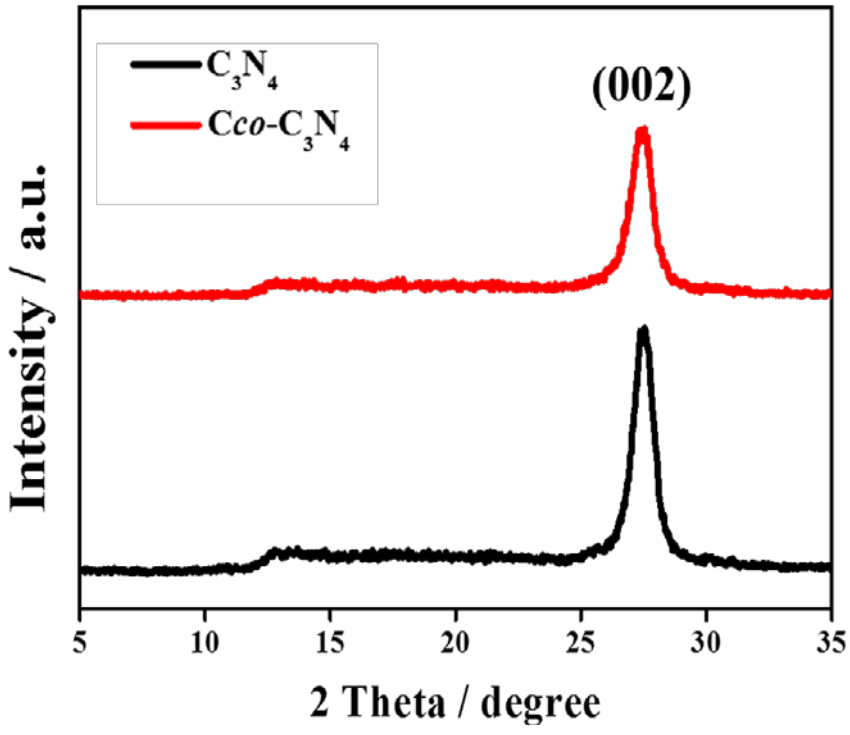

Figure S5. Powder XRD patterns of C_{co}-C_3N_4 and pristine g-C_3N_4. Related to Figure 1 and Figure 3.

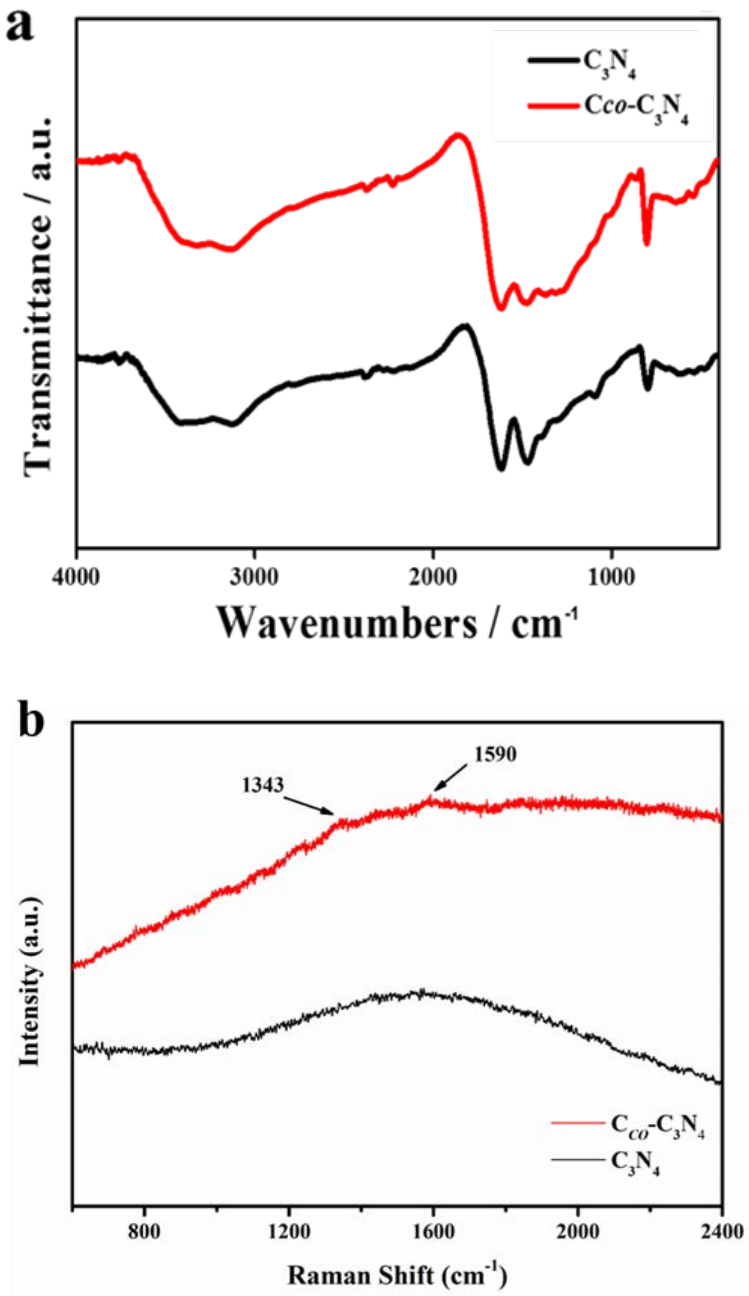

Figure S6. (a) The FT-IR spectra of C_{co}-C_3N_4 and pristine g-C_3N_4. (b) Raman spectra of C_{co}-C_3N_4 and pristine g-C_3N_4

Vibrations at approximately 1600-1500 cm^{-1} (C=N) and 1500-1200 cm^{-1} (C–N) correspond to the typical stretching modes of CN heterocycles. The characteristic mode of the triazine units is observed at approximately 800 cm^{-1}. The broad bands at approximately 3200 cm^{-1} are indicative of the stretching vibration modes of the -NH groups in triazine units. Related to Figure 2 and Figure 3.

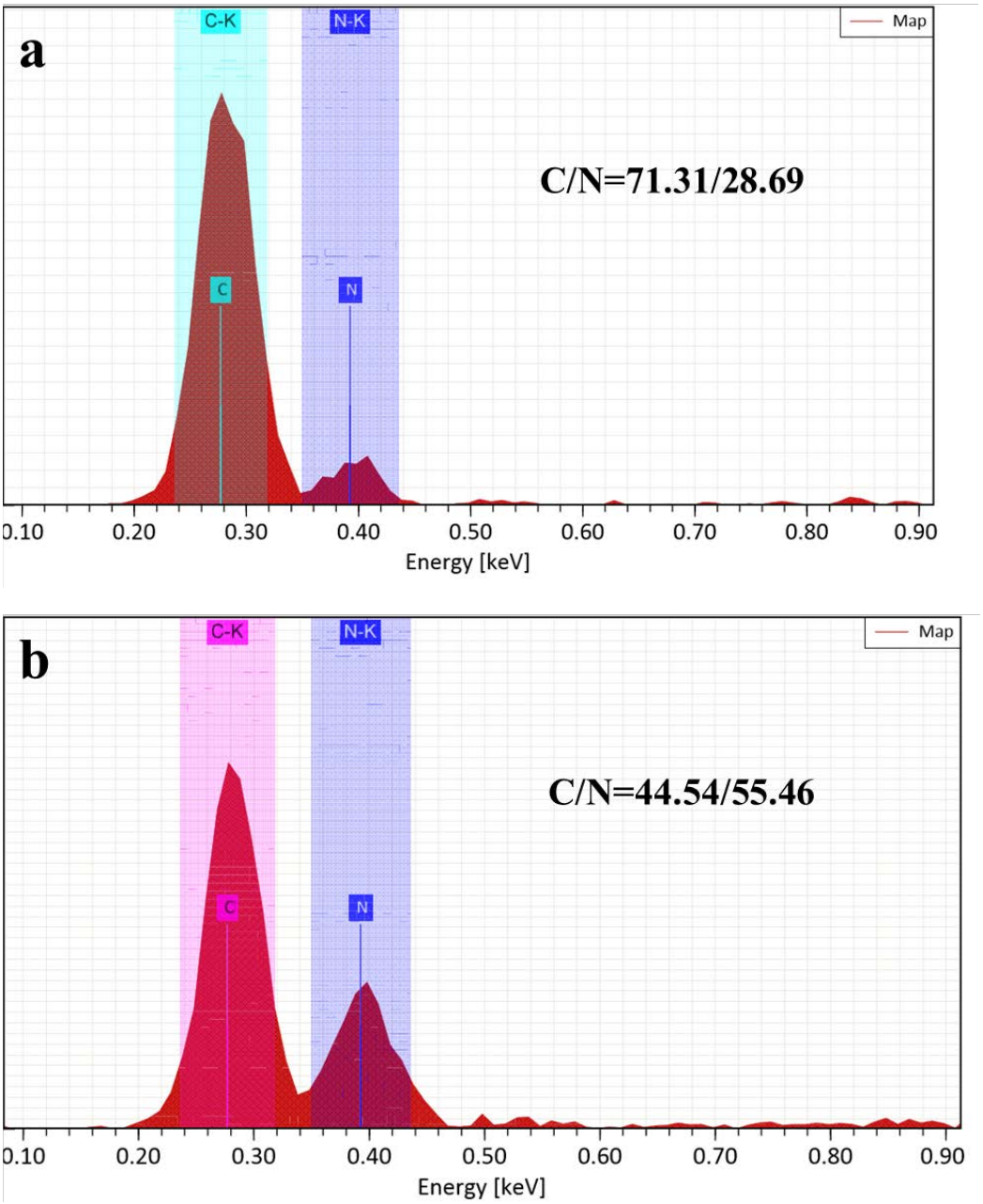

Figure S7. EDS spectra of C_{co}-C_3N_4 (a) and pristine C_3N_4 (b). Related to Figure 3.

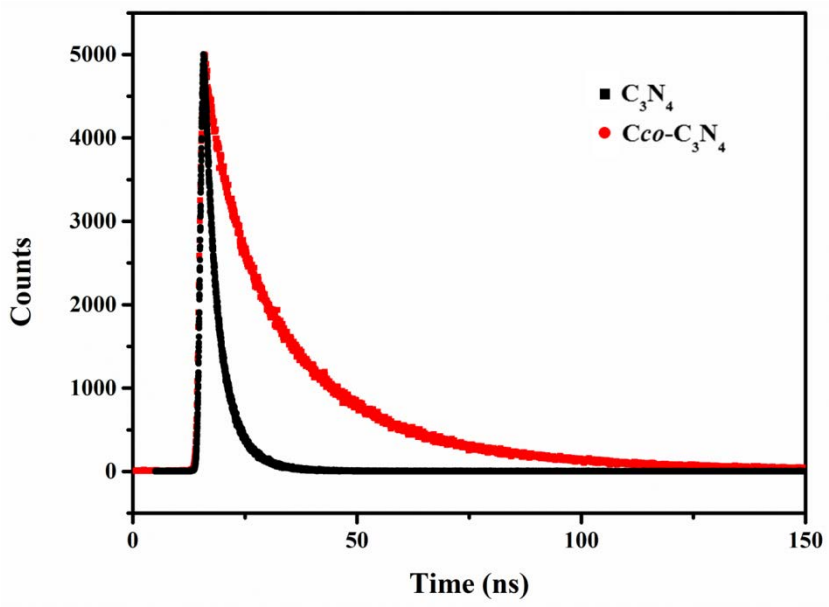

Figure S8. TRPL spectra of C_{co}-C_3N_4 and pristine C_3N_4. Related to Figure 5.

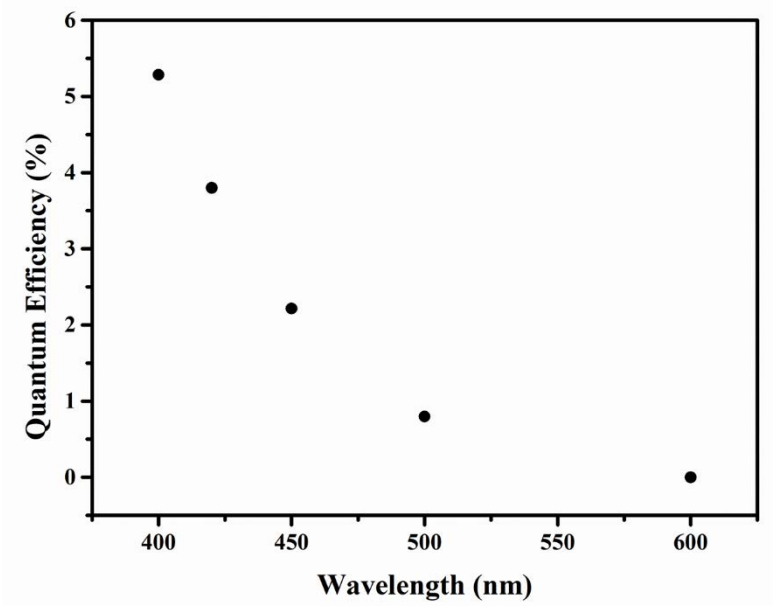

Figure S9. Photocatalytic quantum efficiency of C_{co}-C_3N_4. Related to Figure 4a.

Table S2. Summary of the overall water splitting performance of g-C_3N_4 based catalysts. Related to Figure 4a.

Catalysts	Cocatalysts	Light source	Incident light (nm)	H_2 rate (μmol/h·g)	O_2 rate (μmol/h·g)	Ref.
C_{CO}-C_3N_4	/	300 W Xe lamp	>300 nm	530	255	this work
g-C_3N_4	/	300 W Xe lamp	>300 nm	can't be detected		this work
(C_{ring})-C_3N_4	3 wt% Pt	300 W Xe lamp	>300 nm	371	184	1
g-C_3N_4	3 wt% Pt 1 wt% Co	300 W Xe lamp	>300 nm	61	31	2
C-dot/ C_3N_4	/	300 W Xe lamp	>420 nm	575	/	3
polypyrrole (PPY)/ C_3N_4	3 wt% Pt	300 W Xe lamp	>400 nm	154	/	4
⟨-Fe_2O_3/ 2D-C_3N_4	3 wt. % Pt/2D-C_3N_4 3 wt. % RuO_2/ Fe_2O_3	300 W Xe lamp	>400 nm	38.2	19.1	5
Co-phosphide/ PCN	/	300 W Xe lamp	>300 nm	401.3	204.6	6
Pt-CoP/ g-C_3N_4	3% Pt 3% CoP pH=3	300 W Xe lamp	>400 nm	26.25	12.5	7

TRANSPARENT METHODS

The synthesis of cocrystals: A mixture of melamine (2 mmol, 0.252 g), terephthalic acid (1 mmol, 0.166 g), and water (80 mL) was sealed in a 100 mL Teflon reactor, kept under autogenous pressure at 140 °C for 24 h, and then cooled with a speed of 5 °C/min to room temperature. Colorless sheet-like cocrystals were filtered off, washed with distilled water, and dried in 40 °C drying baker for overnight to entirely remove water.

The synthesis of C_{co}-C_3N_4: The sheet-like cocrystals were placed in a crucible with a cover. It was heated in pipe furnace with a heating rate of 10 °C/min to the target temperatures (500 °C) and maintained for 2 hours in the N_2 flow. After cooling down to room temperature, it was heated again under 550 °C for 2 hours. Finally, the product with brown-color **(Figure S2a)** was obtained and grinded into fine powder for further use. It was observed that the sample weight has decreased during the first steps. When the nanosheets were prepared by thermal oxidation etching, there is almost no degradation. Using a quartz boat covered with a lid could largely reduce the loss of the sample.

The synthesis of pristine g-C_3N_4: According to the literature, pristine g-C_3N_4 was synthesized by thermal treatment. Melamine was placed in a crucible with a cover. It was heated in pipe furnace with a heating rate of 5 °C/min to the target temperatures (550 °C) and maintained for 2 hours in the N_2 flow. After cooling down to room temperature, the final yellow-colored product **(Figure S2b)** was collected. It was grinded into fine powder for further use.

Structural and morphology characterization: For the single crystal X-ray diffraction, the data was obtained using an Oxford Diffraction SuperNova area-detector diffractometer equipped with graphite monochromatized Mo Kα radiation (λ = 0.71073 Å) at room temperature using the T-scan technique. CrysAlisPro[8] was used for the data collection, data reduction and empirical absorption correction. The crystal structure was solved by direct methods, using SHELXS-2014[9] and least-squares refined with SHELXL-2014 using anisotropic thermal

displacement parameters for all non-hydrogen atoms. Details of the crystal are summarized in Table S1.

Powder XRD patterns of all compounds were collected on a Rigaku Ultima-IV automated diffraction system with Cu Kα radiation (λ = 1.5406 Å). Measurements were made in a 2θ range of 5°-45° at room temperature with a step of 0.02° (2θ) and a counting time of 0.2 s/step. The operating power was 40 kV, 50 mA.

Photoluminescence (PL) experiments were conducted on an Edinburgh FLS980 fluorescence spectrometer. IR spectra were recorded in the range of 4000-400 cm^{-1} on a Tensor OPUS (Bruker) FT-IR spectrometer. UV-vis absorption spectra were performed on a UV-vis spectrophotometer (UV3600, Shimadzu) using $BaSO_4$ as the reference. X-ray photoelectron spectrometry (XPS) was recorded using Al Kα radiation (Thermo VG ESCALAB MK II). The positions of all BEs were calibrated by using the C 1s line at 284.8 eV. The Raman spectra were analyzed using a LabRAM instrument (Horiba Jobin Yvon(HJY)) with 532 nm laser excitation.

Scanning electron microscopy with an accelerating voltage of 10 kV (FESEM, S-8010, Hitachi) was applied for detailed morphology analyses and EDS mappings. Transmission electron microscopy (TEM) and high-resolution transmission electron microscopy (HRTEM) analysis were performed on a JEM-2100F microscope at an acceleration voltage of 200 kV.

Photocatalytic hydrogen production: The photocatalytic hydrogen production experiment was conducted in an online photocatalytic hydrogen production system (AuLight, Beijing) at ambient temperature (20 °C). 0.03 g catalyst was suspended in a mixture of 80 mL distilled water in the reaction cell by using a magnetic stirrer. The mixture was deaerated by evacuation to remove O_2 and CO_2 dissolved in water. A Xenon 300 W lamp (CEL-HXF300, AuLight) was used as light irradiation source. The generated hydrogen and oxygen were measured by a gas chromatograph (GC) equipped with a thermal conduction detector (TCD, 5 Å molecular sieve columns with 3 m length) using Ar as carrier gas with flow rate of 20

mL/min. Once the photocatalytic reaction of a testing cycle of 6 h was completed, the reactor was degassed in vacuum before starting the subsequent cycle.

The apparent quantum efficiency (QE) was measured under the same photocatalytic reaction condition. Several band-pass filters (FWHM=15 nm) were employed to achieve a different incident light wavelength under a 300 W Xe lamp for measurement of the QE. The irradiation area was controlled as 23.75 cm^2, and the QE was calculated according to the equation[3] (1):

$$QE = \frac{\text{number of reacted electrons}}{\text{number of incident photons}} = \frac{\text{number of evolved } H_2 \text{ molecules} \times 2}{\text{number of incident photons}} \quad (1)$$

Electrochemical measurement methods: Electrochemical measurements were performed using an electrochemical workstation (CHI 660E, CH instrument Co. USA) with a standard three-electrode photoelectrochemical cell and was used to record transient photocurrent behavior of the samples, where the prepared electrodes immersed in a sodium sulfate electrolyte solution (0.5 M), a gauze platinum and Ag/AgCl (saturated KCl) act as the working, auxiliary, and reference electrode, respectively. The working electrodes were prepared as follows: First, fluoride tin oxide (FTO) glass was washed sequentially with acetone, ethanol and DI water in an ultrasonic bath for 30 min. Next, 0.05 g of photocatalyst was ground with 5 uL of nafion (5 wt%, Alfa Aesar) and mixed with 2 mL of acetone under sonication for 30 min to obtain slurry. Then, the slurry was coated onto a 1 cm × 2 cm FTO glass electrode by the spin coater. After air-drying, the electrodes were sintered at 300 °C for 120 min to improve adhesion. In addition, the three electrodes were immersed in a sodium sulfate electrolyte solution (0.5 M) as conductive media at pH 6.8, which was continuously in an N_2-purged flow to remove O_2 before light irradiation. Photocurrent measurements utilized a 300 W Xe lamp. The working electrode was back-illuminated through the FTO glass in order to minimize absorption by the dark and thick catalyst layer. Capacitance was measured to obtain Mott-Schottky plots for working electrodes at potential window ranged from -1.0 to -0.2 V, and the perturbation signal was an AC voltage magnitude of 50 mV with the frequency at 1, 2 and 3 kHz. The electrochemical impedance spectroscopy (EIS) was

measured at -1.2 V (vs. RHE), and the perturbation signal was also 5 mV with the frequency ranged from 0.01 Hz to 100 kHz. The photoresponse of the prepared photoelectrodes (I-t) was operated by measuring the photocurrent densities under chopped light irradiation (light on/off cycles: 30s) at a bias potential of -0.4 V vs. Ag/AgCl. The transient open-circuit voltage decay (OCVD) measurements were taken for 800 s in all, and the light on and off were controlled at 400 s and 500 s from the start, respectively. The average lifetime of the photogenerated carriers were obtained from the OCVD according to Equation (2):

$$\tau_n = -\frac{k_B T}{q}\left(\frac{dV_{oc}}{dt}\right)^{-1} \quad (2)$$

where k_B is the Boltzmann constant, T is the temperature (in Kelvin), and q is the unsigned charge of an electron.

REFERENCES

1 Che, W., Cheng, W., Yao, T., Tang, F., Liu, W., Su, H., Huang, Y., Liu, Q., Liu, J., Hu, F., Pan, Z., Sun, Z., and Wei, S. (2017). Fast photoelectron transfer in (C_{ring})-C_3N_4 plane heterostructural nanosheets for overall water splitting. J. Am. Chem. Soc. *139*, 3021–3026.

2 Zhang, G., Lan, Z. A., Lin, L., Lin, S., and Wang, X. (2016). Overall water splitting by Pt/g-C_3N_4 photocatalysts without using sacrificial agents. Chem. Sci. *7*, 3062–3066.

3 Liu, J., Liu, Y., Liu, N., Han, Y., Zhang, X., Huang, H., Lifshitz, Y., Lee, S.T., Zhong, J., and Kang, Z. (2015). Metal-free efficient photocatalyst for stable visible water splitting via a two-electron pathway. Science *347*, 970–974.

4 Sui, Y., Liu, J., Zhang, Y., Tian, X., and Chen, W. (2013). Dispersed conductive polymer nanoparticles on graphitic carbon nitride for enhanced solar-driven hydrogen evolution from pure water. Nanoscale *5*, 9150–9155.

5 She, X., Wu, J., Xu, H., Zhong, J., Wang, Y., Song, Y., Nie, K., Liu, Y., Yang, Y., Rodrigues, M.T.F., Vajtai, R., Lou, J., Du, D., Li, H., and Ajayan, P.M. (2017). High

efficiency photocatalytic water splitting using 2D α-Fe_2O_3/g-C_3N_4 Z-scheme catalysts. Adv. Energy Mater. *7*, 1700025.

6 Liu, W., Cao, L.L., Cheng, W.R., Cao, Y.J., Liu, X.K., Zhang, W., Mou, X.L., Jin, L.L., Zheng, X.S., Che, W., Liu, H.Q., Yao, T., and Wei, S.Q. (2017). Single-site active cobalt-based photocatalyst with a long carrier lifetime for spontaneous overall water splitting. Angew. Chem. Int. Ed. *56*, 9312–9317.

7 Pan, Z., Zheng, Y., Guo, F., Niu, P., and Wang, X. (2017). Decorating CoP and Pt nanoparticles on graphitic carbon nitride nanosheets to promote overall water splitting by conjugated polymers. ChemSusChem *10*, 87–90.

8 CrysAlisPro, Rigaku Oxford Diffraction, Version 1.171.39.6a.

9 Sheldrick, G.M. (2008). A short history of SHELX. Acta Crystallogr. Sect. A. *64*, 112–122.